universe

IMPACT FACTOR 2.6

CITESCORE 5.2

Review

Numerical Tools for Electroweak Phase Transition

Xinran Zeng and Yang Zhang

Special Issue

Search for New Physics Through Combined Approaches

Edited by

Dr. Yang Zhang and Prof. Dr. Fei Wang

MDPI

https://doi.org/10.3390/universe12030073

universe

MDPI

Review

Numerical Tools for Electroweak Phase Transition

Xinran Zeng [1] and Yang Zhang [2,*]

[1] School of Physics, Zhengzhou University, Zhengzhou 450001, China; 15038164393@163.com
[2] School of Physics, Henan Normal University, Xinxiang 453007, China
* Correspondence: zhangyang2025@htu.edu.cn

Abstract

The electroweak phase transition serves as a crucial portal to explore physics beyond the Standard Model, with profound implications for gravitational waves, baryogenesis, dark matter, and vacuum stability. We review the computational workflow for analyzing cosmological phase transitions, which includes constructing the finite-temperature effective potential, identifying possible phases, tracing transition history, calculating transition rates, milestone temperatures, and thermal parameters, as well as the numerical tools developed for each step. We compare the functionalities, strategies, and applicable scopes of these tools, aiming to provide a practical guide that helps researchers select the most appropriate computational resources for their studies.

Keywords: electroweak phase transition; beyond the standard model; baryogenesis; gravitational waves

1. Introduction

The Standard Model (SM) of particle physics, while remarkably successful, leaves several fundamental questions unanswered, including the nature of dark matter (DM), the origin of the observed baryon asymmetry of the universe, and the dynamics of cosmic inflation [1–5]. These mysteries strongly suggest the existence of physics beyond the Standard Model (BSM). Since direct searches for new particles at the Large Hadron Collider (LHC) have not yet produced strong evidence [5–12], a variety of alternative approaches are gaining traction.

The discovery of gravitational waves [13,14] opens a new avenue for exploring BSM. The operational ground-based interferometer [15–17], the pulsar timing arrays [18–21], the upcoming space-based interferometers [22–24] and various tabletop experiments [25,26] cover gravitational wave signals across different frequency bands. In BSM, one of the most motivated sources of gravitational waves are electroweak first-order phase transitions (EWPT) in the early universe [27–30]. In such an epoch, the Universe decays from a symmetric, high-temperature phase into the Higgs-broken vacuum, low-temperature phase and forms bubbles spontaneously in the thermal plasma. With the expansion of bubbles, they collide and merge with each other and convert the whole spacetime into the stable vacuum. The collision of bubble walls, the subsequent sound waves, and magnetohydrodynamic turbulence act as sources of gravitational radiation, leading to a stochastic GW background. Within the SM framework, the EWPT is typically a smooth crossover [31], lacking significant observational consequences. However, numerous BSM scenarios, such as those with extended Higgs sectors or new scalar fields, can profoundly alter the nature of this transition, making it a strong first-order phase transition (FOPT) [32–37].

Academic Editor: Douglas Singleton

Received: 28 January 2026
Revised: 25 February 2026
Accepted: 3 March 2026
Published: 5 March 2026

Moreover, a strong FOPT is a prerequisite for electroweak baryogenesis, a compelling mechanism to explain the matter-antimatter asymmetry [38,39]. The properties of the phase transition are also intimately linked to questions of vacuum stability [40–43] and can influence the production mechanism for dark matter [44–53]. Consequently, the study of the EWPT provides a powerful and complementary pathway to BSM physics, connecting particle theory to cosmic physics.

Figure 1 shows the pathway for investigating phase transitions in BSM models. It begins with the Lagrangian of specific physics model, proceeds to calculate the tree-level scalar potential V_{tree}, field-dependent masses, thermal corrections and then constructs the finite-temperature effective potential V_{eff}. This potential, which is a function of the classical fields, serves as the foundational input. The first analytical step is to identify all minimums of the effective potential across a range of temperatures to map out all possible phases. The core task then is to determine the possible phase transitions between these phases, particularly FOPT. The critical temperature T_C (at which the two phases have degenerate potential) and the order parameter γ are straightforward to compute. However, determining additional milestone temperatures and corresponding phase transition parameters is more involved. A key step is the calculation of transition rates per unit time Γ, which depends on evaluating the bounce action S_E and requires solving a set of partial differential equations. Once the transition rates are obtained, one can proceed to compute the nucleation temperature T_N (at which one bubble nucleates per Hubble volume), the percolation temperature T_P (at which the bubbles form an connected network), and the completion temperature T_F (at which the universe essentially completes the transition). Finally, at these characteristic temperatures, thermal parameters such as the transition strength α, the inverse duration of the transition β, and the bubble-wall velocity v_w can be evaluated. With all these phase-transition quantities determined, the results can be used for gravitational-wave prediction, baryogenesis, dark-matter studies, and vacuum-stability analyses.

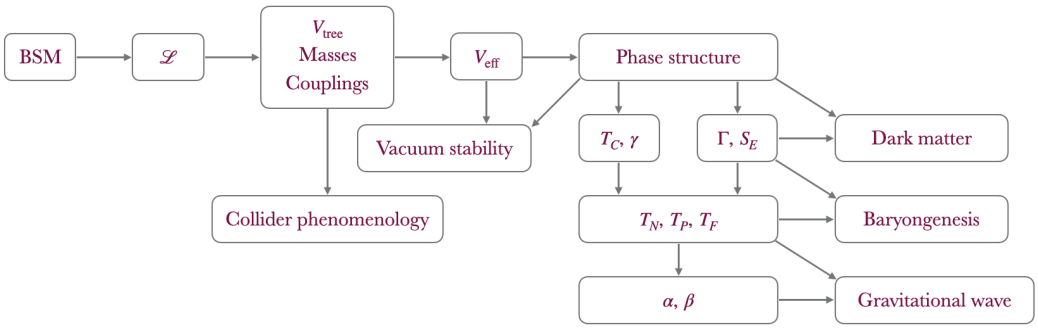

Figure 1. The Workflow for performing a phase transition phenomenological study in BSM theories.

In recent years, various sophisticated software packages have been developed to streamline these calculations, mitigate the risk of manual errors, and enhance the reliability of results. This review aims to provide an overview the prevalent numerical tools dedicated to the study of the electroweak phase transition. We will focus on widely-used packages including `CosmoTransitions_v2.0.6` [54], `BSMPT_3.1.13` [55–57], `PhaseTracer_2.2.0` [58,59], `TransitionListener` [60], `PT2GWFinder_1.1.0` [61], `ELENA` [62], `AnyBubble_2.0.4` [63], `BubbleProfiler_1.0.1` [64], `SimpleBounce_1.0` [65], `FindBounce_1.2.0` [66], `TransitionSolver` [59], `Vevacious_1.2.03` [67], `thermal_funcs` [68], `DRalgo_1.3.0` [69], `WallGo_1.1.1` [70,71], `BubbleDet_1.0.7` [72], as well as an unnamed code [73]. This review seeks to serve as a practical guide for researchers in selecting the appropriate tools for their specific investigations.

In Table 1, we briefly list the key features of numerical tools for analyzing cosmological phase transitions, including `CosmoTransitions`, `BSMPT`, `PhaseTracer`, `Transi-`

tionListener, PT2GWFinder, ELENA and TransitionSolver. Additionally, AnyBubble, BubbleProfiler, SimpleBounce, and FindBounce are designed to solve the bounce equations, compute the bounce action and the bubble profile. thermal_funcs can be used for calculating thermal functions. DRalgo and the codes in Ref. [73] are employed to calculate the bubble wall velocity. BubbleDet computes the prefactor in the transition rate. In the following sections, we will discuss these tools in detail.

Table 1. Key features of numerical tools for analyzing cosmological phase transitions.

Software	Effective Potential	Phase History	Bounce Action Calculation	T_N Formula Reference	T_P Support
CosmoTransitions	$\overline{\text{MS}}$ scheme	Tracing	Path deformation	Equation (20)	No
BSMPT	Multi-Higgs models	Bisection (V1/V), Tracing (V3)	Path deformation	Equation (18)	Yes
PhaseTracer	Various renormalization schemes (Linkable to BSMPT, FlexibleSUSY)	Tracing	Path deformation Based on BubbleProfiler	Equation (20)	Yes
TransitionListener	Based on CosmoTransitions	Tracing	Based on CosmoTransitions	Equation (19)	No
PT2GWFinder	Linkable to Dralgo	Tracing	Based on FindBounce	All available choices	Yes
ELENA	Based on CosmoTransitions	Tracing	Tunneling potential formalism (single-field potentials)	Equation (17)	Yes

2. Effective Potential

The perturbatively calculated effective potential is built upon the tree-level classical potential, V_0, from the Lagrangian. Zero-temperature radiative corrections are then included via the sum of connected, loop level one-particle irreducible diagrams at zero external momentum. These corrections are notably dependent on the choice of gauge and renormalization scheme [74,75]. In the standard approach using the Landau gauge and $\overline{\text{MS}}$ scheme, the one-loop contribution takes the form [74,76,77]:

$$V_1^{T=0}(\phi) = \frac{1}{64\pi^2}\sum_i (-1)^{2s_i}(1+2s_i)m_i^4(\phi)\left[\log\left(\frac{m_i^2(\phi)}{\mu^2}\right) - k_i\right] \tag{1}$$

where the sum extends over all degrees of freedom (real scalar, fermion and vector boson), s_i denotes the spin of field i, and k_i is $\frac{3}{2}$ for scalars and fermions and $\frac{6}{5}$ for gauge bosons. The background field is denoted by ϕ, $m_i(\phi)$ are the field-dependent masses, and μ is the renormalization scale.

The finite-temperature corrections to the effective potential in the Landau gauge can be written in terms of the thermal function [77–79]

$$V_1^T(\phi) = \frac{T^4}{2\pi^2}\left[\sum_i n_{\phi_i} J_B\left(\frac{m_{\phi_i}^2}{T^2}\right) + \sum_j n_{V_j} J_B\left(\frac{m_{V_j}^2}{T^2}\right) - \sum_k n_{f_k} J_B\left(\frac{m_{f_k}^2}{T^2}\right)\right], \tag{2}$$

where $n_{i,j,k}$ denote the degrees of freedom, taken as 1 for scalar fields, 3 for massive vector bosons, 2 for massless vector bosons, and 2 for fermion fields. The thermal function is defined as

$$J_{B/F}(y^2) = \int_0^\infty \mathrm{d}k\, k^2 \log\left[1 \mp e^{-\sqrt{k^2+y^2}}\right]. \tag{3}$$

The finite-temperature perturbation theory breaks down at high temperatures. This issue can be addressed by resumming the leading infrared-divergent contributions, such as the Parwani method [80] and the Arnold–Espinosa method [81]. To this end, we need to obtain the temperature-corrected masses, namely the Debye masses. These masses are de-

rived from the high-temperature expansion of finite-temperature self-energies for diagrams with zero Matsubara modes, in the limit of vanishing momenta. At the one-loop order within the Parwani framework, resummation is achieved by replacing the tree-level masses appearing in the J_B functions with Debye masses for each contributing boson. The Arnold–Espinosa procedure replaces the mass parameters in the high-temperature expansion of the finite-temperature potential with thermal masses. An alternative approach to resolving infrared divergences is to integrate out the temperature dependence by matching to a three-dimensional effective field theory (3DEFT) [82,83]. The three-dimensional theory contains only zero Matsubara modes at the matching scale, and temperature dependence is introduced through the coupling determined by the matching conditions. This method yields higher precision and smaller uncertainties when the transition temperature is much larger than the relevant field scale [84–86].

The effective potential is the main input for most phase transition tools, though it is usually unnecessary to derive the full expression from scratch. `Vevacious` and `DRalgo` can automatically construct an effective potential. `Vevacious` is a tool designed for studying vacuum stability, not phase transitions, but both analyses are based on the same effective potential. It can import model files generated by the Mathematica [87] package `SARAH` [88]. Since the tool focuses on low-temperature physics, Daisy resummation [80,81] is not required. `DRalgo` is designed to automate the construction of 3DEFT for high-temperature phase transitions. It is done by specifying the gauge group, particle representations (scalars, fermions, gauge bosons), along with their respective charges and spinors. Based on these inputs, it then constructs the tree-level scalar potential and the Yukawa/fermion mass terms, and finally executes the dimensional reduction pipeline. `PT2GWFinder` offers an interface with DRalgo, by implementing the helper file `DRTool` to uses dimensionally-reduced potentials.

In `CosmoTransitions`, the formulas for one-loop zero-temperature contributions Equation (1), finite-temperature contributions Equation (2), and thermal functions Equation (3) are already implemented. Thus, users only need to input the expressions for the tree-level potential and field-dependent masses. By default, the infrared divergences at high temperature is not included, so it does not require the expressions of Debye masses. The thermal functions $J_{B/F}$ are calculated via direct numerical integration in the `Python` 3.11 library `SciPy` [89]. To speed up repeated evaluations, the results of direct integration are stored as a grid of precomputed values. Cubic interpolation is then used to quickly estimate the $J_{B/F}$. `ELENA` constructs the finite-temperature scalar potential using the model class in `CosmoTransitions`, and `TransitionListener` is built upon `CosmoTransitions` and extends its effective potential by incorporating contributions from daisy diagrams.

`C++` library `thermal_funcs` [68,90] implements fast and accurate computations of thermal functions $J_{B/F}$ —along with their first and second derivatives with respect to y^2 in Equation (3). It supports six complementary numerical methods tailored to different ranges of y^2: numerical quadrature, Bessel function summation, Taylor expansion, asymptotic representations using Hurwitz zeta functions and polylogarithms, leading-order approximations, and asymptotic bounds. Figure 2 shows the function J_B (left panel) and its derivative near y^2 (right panel), computed using different methods in `thermal_funcs` as well as in `CosmoTransitions`. The `Quad` method performs numerical quadrature, employing the `QUADPACK` [91] algorithms from the `GNU Scientific Library` to treat singularities in the integrand. The results are in agreement with the interpolation from CosmoTransitions over most of the region, except near $y^2 = 0$ where discrepancies in the derivative are observed. Thus, we also show the outcome of the Taylor expansion, which is accurate near $y^2 = 0$ but fails away from it. This comparison demonstrates that the results from the

`Quad` method are more reliable. The error near $y^2 = 0$ can lead to wrong results in specific scenarios, such as the spurious identification of a minimum in the effective potential.

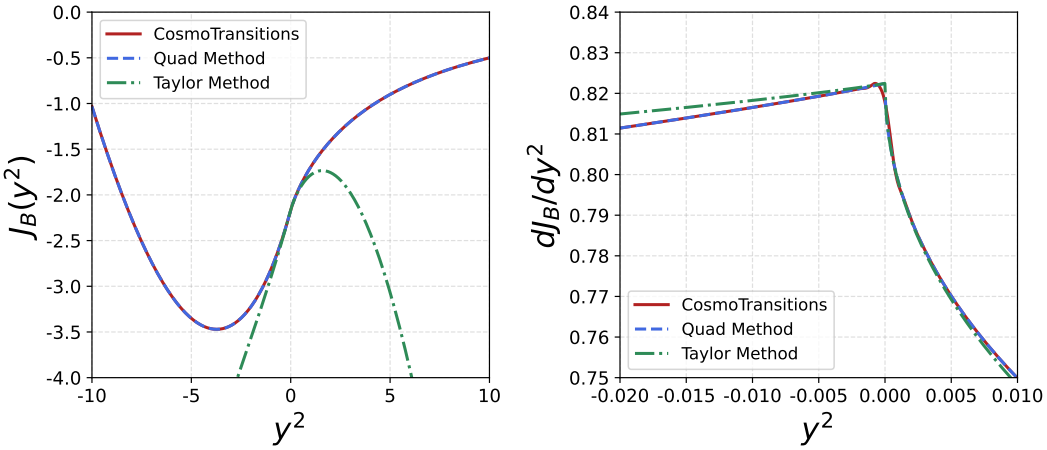

Figure 2. Thethermal function J_B and its derivative calculated using `CosmoTransitions` (red line), as well as `thermal_funcs` with the `Quad` method (blue dash line) and the `Taylor` method (green dot line).

`BSMPT` is well-suited for multi-Higgs models and accepts input parameters from `ScannerS` [92]. It provides implementations of the CP-conserving 2-Higgs-Doublet Model (2HDM), the CP-violating 2HDM [56,93], and the Next-to-Minimal 2HDM [94]. Additionally, the code includes several analytically tractable potentials for validation, the CxSM and the example model from `CosmoTransitions`.

`PhaseTracer` offers a potential input mode similar to that of `CosmoTransitions`, but with an expanded set of features. It supports both the Parwani procedure and the Arnold–Espinosa procedure to handle infrared divergences at high temperature, the $\overline{\text{MS}}$ scheme, on-shell-like schemes in R_ξ gauge, and calculations in covariant gauge. The gauge-independent $\hbar$-expansion method [74,85,95–100] is also implemented. `PhaseTracer` can be linked to `FlexibleSUSY` [101] and `BSMPT`. The latest version provides several example models, including the two-dimensional test potential from `CosmoTransitions`, the dimensionally-reduced Abelian Higgs model implemented in `DRalgo` [69], the Z_2 scalar singlet model under various renormalization schemes [75], and the Left-Right symmetric model [102].

3. Phase History

Here a "phase" refers to a vacuum state corresponding to a local minimum of the finite-temperature effective potential. Once the potential is specified, the workflow includes finding its local minimums at different temperatures, categorizing these minimums into phases, and searching for possible phase transitions among the identified phases. This procedure will be explained in detail later with an explicit example.

For very simple potentials, such as the high-temperature approximation of models involving one or two scalar fields, the minima can be derived analytically. For example, for the SM extended with a Z_2-symmetric real scalar singlet (xSM), the high-temperature approximation is given by [103],

$$V(\phi_h, \phi_s, T) = \frac{(\mu_h^2 + c_h T^2)}{2}\phi_h^2 + \frac{\lambda_h}{4}\phi_h^4 + \frac{\lambda_{hs}}{2}\phi_h^2\phi_s^2 + \frac{(\mu_s^2 + c_s T^2)}{2}\phi_s^2 + \frac{\lambda_s}{4}\phi_s^4, \tag{4}$$

where ϕ_h and ϕ_s are the background field for the Higgs h and the extended real scalar singlet s, μ_h^2 and μ_s^2 are the coefficient of the quadratic term, λ_h and λ_s are the self-couplings,

and λ_{hs} is the portal coupling that connects the two sectors. c_h and c_s are thermal correction coefficients, arising from contributions of gauge bosons and fermions to the effective potential. There are three extrema,

$$(h_0, s_0) = (0, 0), \quad (h_1, s_1) = (\sqrt{-\frac{\mu_h^2 + c_h T^2}{\lambda_h}}, 0), \quad (h_2, s_2) = (0, \sqrt{-\frac{\mu_s^2 + c_s T^2}{\lambda_s}}). \tag{5}$$

Substituting them back into Equation (4), we can obtain the potentials corresponding to these minimums, thereby deriving the critical temperature T_C at which

$$V(h_1, s_1, T_C) = V(h_2, s_2, T_C). \tag{6}$$

The physical meaning of T_C will be specified later. Here it is given by

$$T_C^2 = \frac{\lambda_h c_s \mu_s^2 - \lambda_s c_h \mu_h^2 - \sqrt{\lambda_h \lambda_s} |c_s \mu_h^2 - c_h \mu_s^2|}{\lambda_s c_h^2 - \lambda_h c_s^2} \tag{7}$$

This analytical approach is restricted to potentials of simple form. There are some examples of simple potential in `BSMPT v3`.

For potentials incorporating full loop corrections, obtaining the minimums analytically becomes infeasible, necessitating the use of numerical methods. `BSMPT v1` uses a bisection method for calculating T_C, which is efficient and robust if there is only a single transition between two phases. Figure 3 demonstrates the iterative bisection procedure for locating T_C. The algorithm operates on a temperature interval $[T_{\text{Low}}, T_{\text{High}}]$ that is guaranteed to contain T_C. By iteratively evaluating the global minimum at the midpoint T_{Mean} and updating the interval bounds based on its location (relative to the origin), the search range is systematically refined until it converges to T_C. This method is widely used in models with simple phase histories, such as the Abelian Higgs example in `DRalgo`.

This bisection method breaks down if the thermal history contains more than one FOPT, or if one aims to study a transition between two phases where neither is at the origin. Therefore, packages like `CosmoTransitions`, `ELENA`, `TransitionListener`, `PhaseTracer`, and `BSMPT v3` trace the full evolution of minimums with changing temperature.

As shown in Figure 4, this method begins at a minimum corresponding to an extreme temperature—for instance, the non-zero minimum (black dot) in the zero-temperature effective potential (purple curve) in the left panel. Starting from this point, we increase the temperature by a step ΔT and estimate the new minimum using the field derivatives with respect to temperature, obtained by solving the Hessian matrix equation. The predicted position is then refined through a local optimization procedure (e.g., the Nelder–Mead method [104]) to locate the precise minimum. If the refined minimum lies sufficiently close to the predicted one, the two are regarded as belonging to the same phase. This minimum is saved, the temperature is increased again, and the process is repeated—this produces the sequence of black points in the right panel. If, instead, the refined minimum is not close to the predicted one, the step ΔT is reduced and a new prediction is made. The step size is decreased when the tracking encounters discontinuities or poor predictions, and increased when the evolution is smooth. Should ΔT be reduced to a prescribed tolerance while the refined minimum remains far from the predicted one, the current phase is considered to have ended. The predicted minimum then corresponds to the onset of a new phase, i.e., the red dot at $T \simeq 126\,\text{GeV}$. From this point, the same tracking procedure is applied both forward and backward in temperature to trace the new phase.

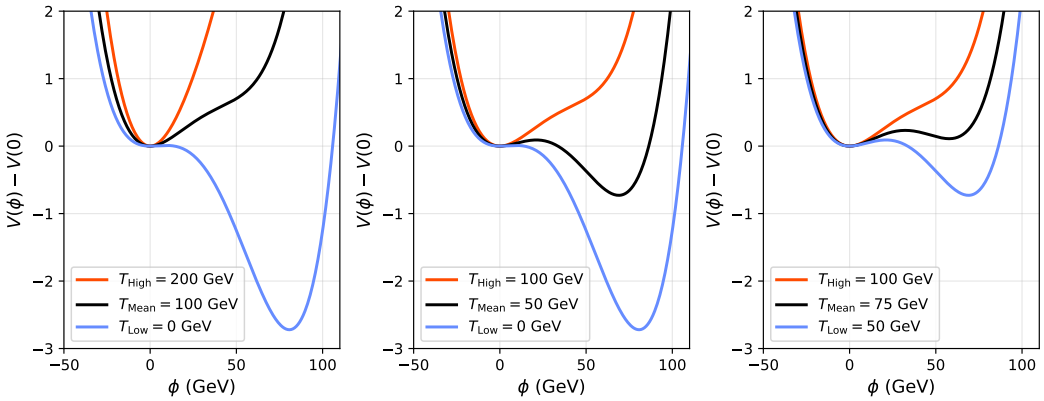

Figure 3. Schematic of the bisection algorithm used to find T_C. The search interval is iteratively refined by updating its bounds based on the location of the global minimum at the midpoint temperature.

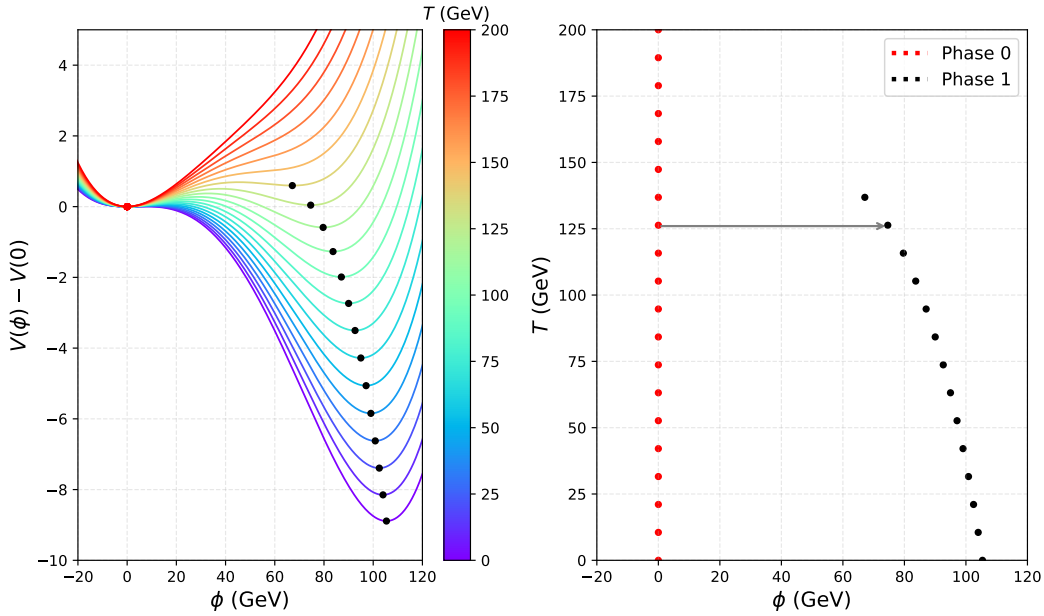

Figure 4. Schematic of the tracing algorithm used to find phases and T_C. (**Left**): Effective potentials at different temperatures (colored curves). Local minimums are marked by black and red dots. (**Right**): minimums plotted in the ϕ–T plane, classified into two distinct phases. The critical temperature T_C corresponds to the gray arrow.

To explore all possible phases, the above procedure is repeated for each minimum at extreme temperatures. `CosmoTransitions` employs user-provided approximations for the zero-temperature minimums as starting points, whereas `PhaseTracer` seeds its tracing algorithm with 50 random initial positions at both the zero-temperature and the user-specified maximum temperature. After all phases are identified, possible transitions between every two overlapping phases can be determined using the bisection method.

The main challenge in tracing a phase lies in identifying its endpoint, which typically corresponds to a saddle point where the potential is flat in one direction. This implies that the Hessian matrix has an eigenvalue of zero. However, confirming this numerically is difficult because we need a tolerance threshold to decide when a value is effectively zero. The problem is compounded when other eigenvalues are many orders of magnitude larger than the near-zero one, making it impractical to choose a single tolerance that works universally. Another common issue is that the potential may not be smooth due to numerical problems or model construction, leading to spurious local minimums and causing the calculation to fail.

At this stage, we can obtain the order parameter of electroweak FOPT from these tools,

$$\gamma = \frac{v_C}{T_C}, \tag{8}$$

where v_C is the non-zero expectation value of the Higgs at temperature T_C. Successful electroweak baryogenesis requires the EW sphaleron process to be out of equilibrium in the broken phase to ensure that the baryon asymmetry is not washed out. This condition can be translated into an approximate bound $\gamma \gtrsim 1$ [105]. `BSMPT v2` can further calculate the baryon asymmetry of the Universe for the CP-violating 2HDM via two approximations, the semi-classical force approach [38] and the VEV-insertion approximation approach [39].

4. Transition Rates

In the presence of two minimums, the system may tunnel through the potential barrier via quantum effects or overcome it through thermal fluctuations, leading to the formation of bubbles in spacetime. The transition probability per unit time per unit volume at finite-temperature is given by [106,107]

$$\frac{\Gamma}{V} = A(T)e^{-S(T)/T}[1 + \mathcal{O}(\hbar)], \tag{9}$$

where $A(T)$ is a temperature-dependent prefactor and $S_E(T)$ is the Euclidean action,

$$S_E(T) = 4\pi \int_0^\infty \mathrm{d}\rho\, \rho^2 \left[\frac{1}{2}\dot{\phi}^2 + V(\phi)\right]. \tag{10}$$

Here $\rho = \sqrt{\tau^2 + |\vec{x}|^2}$ and $\dot{\phi} = \mathrm{d}\phi/\mathrm{d}\rho$, τ represents the Euclidean (imaginary) time coordinate, $\vec{x}$ denotes the three-dimensional spatial coordinate vector in Euclidean space. The integration is performed over the bounce solution ϕ_b, an instanton that interpolates between the two phases. ϕ_b satisfies the Euler–Lagrange equations

$$\ddot{\phi} + \frac{2}{\rho}\dot{\phi} = \nabla V(\phi), \tag{11}$$

with boundary conditions

$$\dot{\phi}|_{\rho=0} = 0, \quad \phi|_{\rho\to\infty} = \phi_f, \tag{12}$$

implying that the transition occurs at $\rho = 0$, while far away the field remains in the false vacuum ϕ_f.

Accordingly, obtaining the bounce solution corresponds to solving a system of partial differential equations, which is a mathematical problem that remains an active research area. To address this challenge, a variety of numerical algorithms has been developed [108–116]. For one-dimensional potential, the over/under-shooting method proves both accurate and stable [117]. This approach frames the field evolution as a classical particle moving in an inverted potential $-V(\phi)$, where ϕ acts as a spatial coordinate and ρ plays the role of time. It searches an initial field configuration ϕ_0 near the true vacuum ϕ_t, such that the field evolves to settle at the false vacuum ϕ_f as $\rho \to \infty$. This method is widely used in phenomenological studies and is implemented in numerical tools such as `CosmoTransitions`, `BSMPT v3`, `BubbleProfiler`, and `PhaseTracer2`.

For multi-dimensional potentials, the path deformation method proposed in Refs. [54,118] is implemented in tools such as `CosmoTransitions`, `BSMPT v3` and `PhaseTracer2`. This method decomposes the equations of motion into components parallel and perpendicular to an initial guess trajectory, then iteratively deforms the path toward the true bounce solution by applying corrections along the perpendicular direction. `ELENA` adopts the tunneling potential

formalism [112], which converts the problem into an optimization task, offering improved speed and stability. However, it is currently limited to single-field potentials. `Vevacious` and `TransitionListener` relies on `CosmoTransitions` and `PT2GWFinder` uses `FindBounce` to obtain bounce profiles and actions.

Additionally, several dedicated tools have been developed. `FindBounce` implements the polygonal bounce method, a semi-analytic approach that discretizes the potential into piecewise-linear segments [119]. `BubbleProfiler` employs a perturbative technique for multifield potentials [108]. `AnyBubble` utilizes a multiple-shooting method, dividing the time domain into subintervals and stitching together local solutions to construct the global bounce. `SimpleBounce` treats the bounce solution as a fixed point of a gradient-flow equation.

Beyond these approaches, machine learning has also been applied to this problem. Ref. [114] employs neural networks to solve the differential equations relevant to bounce action computations. Ref. [120] trains a neural network to predict the bounce action directly from one-dimensional potentials, using 15 nodal values of the potential as input. Ref. [121] constructs a neural network that maps model parameters directly to the action curve.

A prominent issue in the numerical computation of the action is instability and error. Ideally, the action should vary smoothly with temperature. However, as shown in Figure 5, we usually can observe a zigzag pattern. This irregular behavior will introduce non-negligible errors in the calculation of β/H, which will be introduced later. In addition to improving the computational accuracy of the action, fitting the temperature-dependent action function offers another viable approach. `PhaseTracer2` applies a linear fit near the reference temperature to compute β. `Vevacious` approximates the straight-path Euclidean action S^{straight}—representing the bounce action along a direct path from the false vacuum to the true vacuum—using $(T_C - T)^2$ multiplied by a polynomial in T, in order to estimate an upper bound for the survival probability. `PT2GWFinder` adopts a similar fitting strategy around the critical temperature T_C. Ref. [121] utilize the fitting function across the entire temperature range.

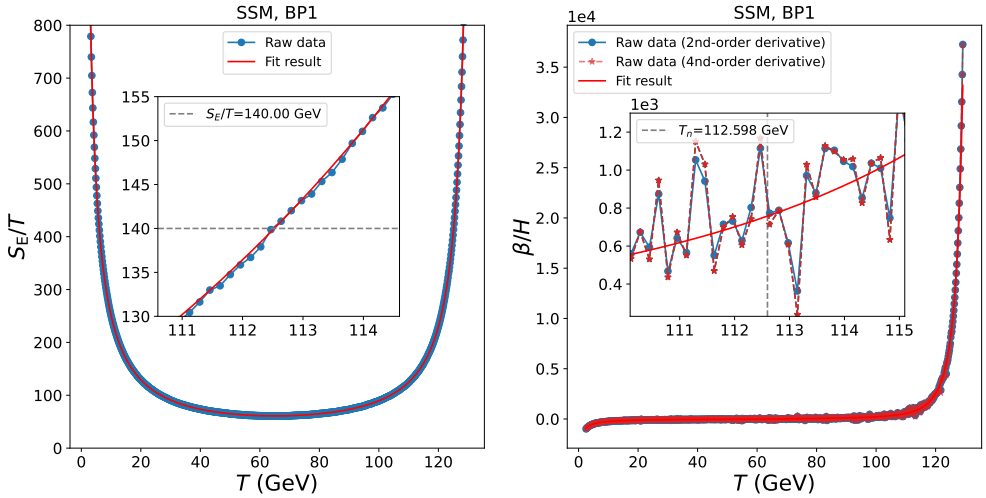

Figure 5. The variation of S/T and β/H with temperature for a example model, where the dotted lines represent the raw data and the solid lines represent the fitting results. This figure is taken from our previous work [121].

The prefactor $A(T)$ in Equation (9) arises from fluctuations around the saddle point. At leading order, these fluctuations contribute a quadratic term to the action and is given by [107,122]

$$A(T) = T\left(\frac{S_E}{2\pi T}\right)^{\frac{3}{2}}\left(\frac{\det'\left[-\nabla^2 + V''(\phi_b)\right]}{\det\left[-\nabla^2 + V''(\phi_f)\right]}\right)^{-\frac{1}{2}}, \tag{13}$$

where $\det'$ stands for the product of all eigenvalues excluding the zeros . `BubbleDet` automatically computes them and regularizes the sums for fluctuating scalar and gauge fields. The calculation related to the determinant term is challenging, so `BSMPT v3`, `PT2GWFinder` and `ELENA` adopts the approximation

$$A(T) \simeq T^4\left(\frac{S}{2\pi T}\right)^{\frac{3}{2}}, \tag{14}$$

while `CosmoTransitions` and `PhaseTracer2` employ a further simplified version, $A(T) \simeq T^4$.

Finally, an important yet often overlooked issue is the discrete symmetry of the potential. As shown in Figure 6, consider two coexisting phases P and Q and their symmetry partners P' and Q' related by a Z_2 discrete symmetry. P, P' are false vacuums and Q, Q' are false vacuums. Four possible phase transitions can occur: $P \to Q$, $P' \to Q$, $P \to Q'$, and $P' \to Q'$. By discrete symmetry, the actions (tunneling barriers) satisfy

$$S(P \to Q) = S(P' \to Q'), \quad S(P' \to Q) = S(P \to Q'), \tag{15}$$

but $S(P \to Q)$ may differ from $S(P \to Q')$. These actions determine which transition the Universe follows. `CosmoTransitions` utilizes a user-defined function to carve out the symmetric field space. `PhaseTracer` selects the transition with the smallest action value to be the one that could have actually occurred in the model's cosmological history. `BSMPT v3` chooses the transitions with the shortest path between false and true vacuum.

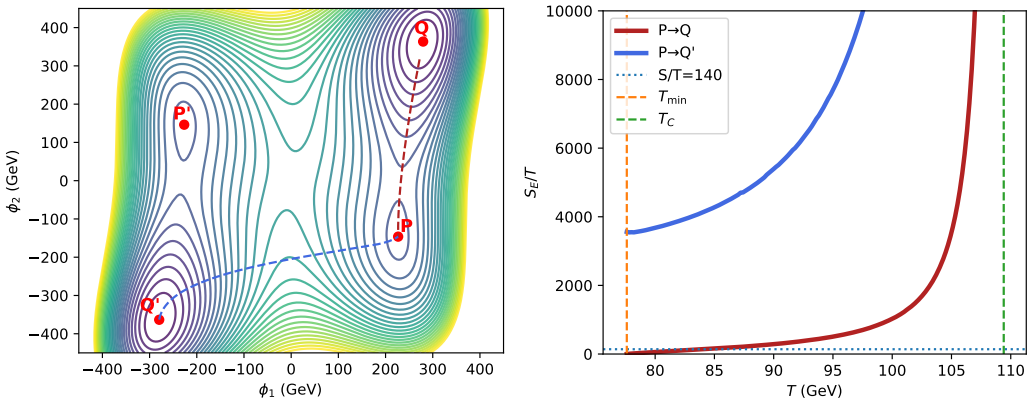

Figure 6. Schematic illustration of Z_2 discrete symmetry in the potential. P and Q denote the false and true vacuums, with P' and Q' representing their symmetry partners. There are two unique transition path and the right panel shows the action curve corresponding to each path. This figure is taken from our previous work [59].

5. Transition Temperatures

In Equation (6), we define the critical temperature T_C as the temperature at which the free energy densities of two phases become equal. It is relatively straightforward to compute, which is why T_C is often treated as the phase transition temperature in simplified estimations. In reality, however, the actual phase transition does not occur at this temperature. The nucleation temperature T_N is a more physically relevant quantity in practice.

The nucleation temperature is defined as the temperature at which, on average, one bubble nucleates per Hubble volume:

$$N(T_N) = \int_{T_N}^{T_C} \frac{\mathrm{d}T}{T} \frac{\Gamma(T) P_f(T)}{H(T)^4} = 1, \tag{16}$$

where $H(T)$ is Hubble parameter and $P_f(T)$ is the false vacuum fraction, given by [123,124]

$$P_f(T) = e^{-\int_{T_0}^{T} \mathrm{d}T' \, \Gamma(T') \frac{a^3(T')}{a^3(T)} \mathcal{V}(T',T)} \tag{17}$$

where $\mathcal{V}(T', T)$ denotes the fractional volume of a bubble at T that nucleated at temperature T'. The fully accurate calculation is rather involved, but since the exponential term in Equation (9) dominates the behavior, the expression can be simplified to

$$\frac{\Gamma(T_N)}{H^4(T_N)} = 1. \tag{18}$$

For electroweak scale transition, it can be further simplified to

$$\frac{S_E}{T_N} \simeq 146 - 2\ln\left(\frac{g_{\mathrm{eff}}^{\mathrm{tot}}}{100}\right) - 4\ln\left(\frac{T_N}{100\,\mathrm{GeV}}\right) \tag{19}$$

$$\simeq 140. \tag{20}$$

where $g_{\mathrm{eff}}^{\mathrm{tot}}$ is the total effective degree of freedom.

`ELENA` utilizes Equation (17) as it is for one scalar potential; `BSMPT v3` adopts Equation (18); `TransitionListener` uses Equation (19); `CosmoTransitions` and `PhaseTracer2` utilize Equation (20); `PT2GWFinder` provides all the choices. Note that, as shown in Figures 5 and 6, the S/T may decrease monotonically as the temperature falls, but this is not always the case. The nucleation temperature is determined by selecting the first time where the condition in Equations (18)–(20) is satisfied.

For strongly supercooled transitions, the Universe remains in the false vacuum long after the vacuum becomes metastable, so cosmic expansion must be accounted for. In this case, the time of bubble collisions may occur much later than the nucleation time. Thus, using the percolation temperature is more reasonable when calculating GWs. The percolation temperature is defined as [125]

$$P_f(t_P) \approx 0.71. \tag{21}$$

Similarly, the completion temperature can be obtained by solving

$$P_f(t_F) = \epsilon, \tag{22}$$

where $\epsilon \ll 1$.

`CosmoTransitions` and `TransitionListener` provides the critical temperature T_C and the nucleation temperature T_N. `BSMPT v3`, `PhaseTracer2` combined with `TransitionSolver`, and `ELENA` are capable of delivering the full set of characteristic temperatures

6. Thermal Parameters

In addition to the transition temperatures, calculating phase transition GWs and baryon asymmetry requires other properties of the phase transition: the characteristic length scale, transition strength, bubble wall velocity, and so on. Here, we only cover the thermal parameters computed by the above tools, while calculations of more parameters, GWs, and baryon asymmetry are beyond the scope of this paper.

As the free energy density $\mathcal{F} = V$ and the pressure $p = -\mathcal{F}$, the energy density ρ, the enthalpy density ω, and the entropy density s are given as

$$\rho = V - T\frac{\partial V}{\partial T}, \quad w = -T\frac{\partial V}{\partial T}, \quad s = -\frac{\partial V}{\partial T}. \tag{23}$$

The coefficient β in the exponential nucleation rate $\Gamma(t) = \Gamma(t_*)e^{\beta(t-t*)}$ characterizes the inverse duration of the phase transition. Expanding the Euclidean action around t_* to first order yields [126]

$$\beta = T_* H_* \frac{d}{dT}\left(\frac{S(T)}{T}\right)\Big|_{T_*}, \tag{24}$$

where T_* is the reference temperature of the transition, and t_* and H_* denote the corresponding time and Hubble parameter at this temperature. `PhaseTracer2`, `PT2GWFinder`, `TransitionListener` and `BSMPT v3` employ it in GWs calculations. Since its computation involves the differential of S, the numerical noise present in the calculation of S, as shown in Figure 6, has a strong impact on its evaluation. Thus, different fitting procedures are adopted in `PhaseTracer2`, `Vevacious` and `PT2GWFinder` to mitigate this issue. In addition, `TransitionSolver` and `ELENA` adopt the mean bubble separation R instead, which is derived from the bubble number density n_B [123]

$$n_B = T^3 \int_T^{T_c} dT' \frac{\Gamma(T')P_f(T')}{T'^4 H(T')}, \quad R = n_B^{1/3}. \tag{25}$$

This approach offers advantages in treating strongly supercooled phase transitions.

The bubble wall velocity v_w is another crucial parameter in gravitational wave predictions. It is time-dependent, as the bubble walls starting at rest and accelerating due to the pressure difference. The acceleration stage is typically short and can often be neglected. Determining the terminal wall velocity requires solving coupled scalar–fluid Boltzmann equations under non-equilibrium conditions, which remains a challenging task. Thus, it is commonly treated as an input parameter in tools such as `PhaseTracer2`, `PT2GWFinder`, `TransitionSolver`, `ELENA` and `BSMPT v3`. The latter two also offer approximate expressions based on Refs. [127,128]. There are also dedicated tools to compute v_w more rigorously. `WallGo` implements the full treatment developed in Ref. [129]. Ref. [73] provides a code based on the local thermal equilibrium approximation.

The strength of FOPT is quantified by α, the fraction of potential energy available for the the production of GWs. For the bag model, the vacuum energy is given by the bag constant ϵ, it is given as [130]

$$\alpha = \frac{4\epsilon}{3w_f(T_*)}, \tag{26}$$

where $w_f(T_*)$ is the enthalpy density far away from the bubble wall. In realistic models, it is usually defined by the trace anomaly as [131]

$$\alpha = \frac{1}{\pi^2 g_* T_*^4/30}\left[V(\phi_f) - V(\phi_t) - \frac{T}{4}\left(\frac{\partial V(\phi_f)}{\partial T} - \frac{\partial V(\phi_t)}{\partial T}\right)\right]_{T=T_*}, \tag{27}$$

where g_* represents the effective number of relativistic degrees of freedom at T_*. `TransitionSolver` implements both Equations (26) and (27); `ELENA` and `TransitionListener` adopts Equation (26); while `PhaseTracer2`, `PT2GWFinder`, and `BSMPT v3` adopt Equation (27), despite slight differences in their respective treatments of g_*.

FOPT in the early Universe generates GWs through bubble wall collisions, sound waves and turbulence in the cosmic fluid. Each mechanism contributes a distinct power spectrum, and the total power spectrum is given by the sum of the three contribu-

tions. The resulting amplitudes and peak frequencies are governed by the phase transition temperature and the thermal parameters introduced above. `PhaseTracer2`, `ELENA`, `TransitionListener`, `BSMPT v3`, `PT2GWFinder` and `TransitionSolver` can output the GW power spectrum using fit formulae from analytic expresions [132–137]. There are also lattice simulation tools for simulating the nonlinear dynamics of the early universe to calculate GWs, such as `CosmoLattice` [138], `HLattice` [139], and `PSpectRe` [140], but these are beyond the scope of this review.

7. Conclusions

The studies of electroweak phase transition connect particle physics beyond the Standard Model to observable cosmological phenomena, including gravitational waves, baryogenesis, dark matter, and vacuum stability. They become particularly important as the direct searches for new physics at the LHC continue to return negative results. These studies drive advances in numerical tools to tackle the needed complex calculations. This review systematically outlines the key tools for analyzing cosmological phase transitions, as summarized in Table 1. It covers the construction of the finite-temperature effective potential, the tracing of phase histories, and the calculation of transition rates, milestone temperatures, and thermal parameters, together with an overview of the numerical tools for each step.

Author Contributions: Conceptualization, Y.Z.; Plotting, X.Z.; writing, X.Z. and Y.Z. All authors have read and agreed to the published version of the manuscript.

Funding: This research was funded by National Natural Science Foundation of China No. 12105248 and No. 12335005.

Data Availability Statement: No new data were created or analyzed in this study.

Conflicts of Interest: The authors declare no conflicts of interest.

References

1. Riotto, A.; Trodden, M. Recent progress in baryogenesis. *Ann. Rev. Nucl. Part. Sci.* **1999**, *49*, 35–75. [CrossRef]
2. Mazumdar, A.; White, G. Review of cosmic phase transitions: Their significance and experimental signatures. *Rep. Prog. Phys.* **2019**, *82*, 076901. [CrossRef] [PubMed]
3. Athron, P.; Balázs, C.; Fowlie, A.; Morris, L.; Wu, L. Cosmological phase transitions: From perturbative particle physics to gravitational waves. *Prog. Part. Nucl. Phys.* **2024**, *135*, 104094. [CrossRef]
4. Cirelli, M.; Strumia, A.; Zupan, J. Dark Matter. *arXiv* **2024**, arXiv:2406.01705. [CrossRef]
5. Navas, S.; Amsler, C.; Gutsche, T.; Hanhart, C.; Hernández-Rey, J.J.; Lourenço, C.; Masoni, A.; Mikhasenko, M.; Mitchell, R.E.; Patrignani, C.; et al. Review of particle physics. *Phys. Rev. D* **2024**, *110*, 030001. [CrossRef]
6. Sopczak, A. Higgs Boson Searches at the LHC Beyond the Standard Model. *Physics* **2024**, *6*, 1132–1170. [CrossRef]
7. Wang, L.; Yang, J.M.; Zhang, Y.; Zhu, P.; Zhu, R. A Concise Review on Some Higgs-Related New Physics Models in Light of Current Experiments. *Universe* **2023**, *9*, 178. [CrossRef]
8. Wang, F.; Wang, W.; Yang, J.; Zhang, Y.; Zhu, B. Low Energy Supersymmetry Confronted with Current Experiments: An Overview. *Universe* **2022**, *8*, 178. [CrossRef]
9. Trocino, D. Searches in the long-lived particle and dark sectors. In Proceedings of the 35th Rencontres de Blois: Particle Physics and Cosmology, Blois, France, 20–25 October 2024.
10. Neutelings, I. Leptoquark searches at ATLAS and CMS. In Proceedings of the 58th Rencontres de Moriond on Electroweak Interactions and Unified Theories, La Thuile, Italy, 24–31 March 2024.
11. Seidita, R. Dark sector searches at ATLAS and CMS. *PoS* **2025**, *489*, 032. [CrossRef]
12. Hirose, S. Search for rare Higgs boson decays and BSM Higgs bosons. *PoS* **2026**, *478*, 186. [CrossRef]
13. Abbott, B.P. et al. [LIGO Scientific Collaboration and Virgo Collaboration] GWTC-1: A Gravitational-Wave Transient Catalog of Compact Binary Mergers Observed by LIGO and Virgo during the First and Second Observing Runs. *Phys. Rev. X* **2019**, *9*, 031040. [CrossRef]

14. Abbott, B.P. et al. [LIGO Scientific Collaboration and Virgo Collaboration] Binary Black Hole Population Properties Inferred from the First and Second Observing Runs of Advanced LIGO and Advanced Virgo. *Astrophys. J. Lett.* **2019**, *882*, L24. [CrossRef]
15. Aasi, J. et al. [LIGO Scientific Collaboration] Advanced LIGO. *Class. Quant. Grav.* **2015**, *32*, 074001. [CrossRef]
16. Acernese, F.; Agathos, M.; Agatsuma, K.; Aisa, D.; Allemandou, N.; Allocca, A.; Amarni, J.; Astone, P.; Balestri, G.; Ballardin, G.; et al. Advanced Virgo: A second-generation interferometric gravitational wave detector. *Class. Quant. Grav.* **2015**, *32*, 024001. [CrossRef]
17. Akutsu, T.; Ando, M.; Arai, K.; Arai, Y.; Araki, S.; Araya, A.; Aritomi, N.; Aso, Y.; Bae, S.; Bae, Y.; et al. Overview of KAGRA: Detector design and construction history. *Prog. Theor. Exp. Phys.* **2021**, *2021*, 05A101. [CrossRef]
18. Xu, H.; Chen, S.; Guo, Y.; Jiang, J.; Wang, B.; Xu, J.; Xue, Z.; Caballero, R.N.; Yuan, J.; Xu, Y.; et al. Searching for the nano-hertz stochastic gravitational wave background with the Chinese pulsar timing array data release I. *Res. Astron. Astrophys.* **2023**, *23*, 075024. [CrossRef]
19. Reardon, D.J.; Zic, A.; Shannon, R.M.; Hobbs, G.B.; Bailes, M.; Di Marco, V.; Kapur, A.; Rogers, A.F.; Thrane, E.; Askew, J.; et al. Search for an isotropic gravitational-wave background with the parkes pulsar timing array. *Astrophys. J. Lett.* **2023**, *951*, 1. [CrossRef]
20. Antoniadis, J. et al. [EPTA Collaboration and InPTA Collaboration] The second data release from the European Pulsar Timing Array—III. Search for gravitational wave signals. *Astron. Astrophys.* **2023**, *678*, A50. [CrossRef]
21. Agazie, G.; Anumarlapudi, A.; Archibald, A.M.; Arzoumanian, Z.; Baker, P.T.; Bécsy, B.; Blecha, L.; Brazier, A.; Brook, P.R.; Burke-Spolaor, S.; et al. The NANOGrav 15 yr Data Set: Evidence for a Gravitational-wave Background. *Astrophys. J. Lett.* **2023**, *951*, L8. [CrossRef]
22. Amaro-Seoane, P.; Audley, H.; Babak, S.; Baker, J.; Barausse, E.; Bender, P.; Berti, E.; Binetruy, P.; Born, M.; Bortoluzzi, D.; et al. Laser Interferometer Space Antenna. *arXiv* **2017**, arXiv:1702.00786. [CrossRef]
23. Hu, W.R.; Wu, Y.L. The Taiji Program in Space for gravitational wave physics and the nature of gravity. *Natl. Sci. Rev.* **2017**, *4*, 685–686. [CrossRef]
24. Luo, J.; Chen, L.-S.; Duan, H.-Z.; Gong, Y.-G.; Hu, S.; Ji, J.; Liu, Q.; Mei, J.; Milyukov, V.; Sazhin, M.; et al. TianQin: A space-borne gravitational wave detector. *Class. Quant. Grav.* **2016**, *33*, 035010. [CrossRef]
25. Schnabel, R.; Korobko, M. Optical sensitivities of current gravitational wave observatories at higher kHz, MHz and GHz frequencies. *Sci. Rep.* **2025**, *15*, 25733. [CrossRef] [PubMed]
26. Carney, D.; Higgins, G.; Marocco, G.; Wentzel, M. Superconducting Levitated Detector of Gravitational Waves. *Phys. Rev. Lett.* **2025**, *134*, 181402. [CrossRef]
27. Cai, R.G.; Cao, Z.; Guo, Z.K.; Wang, S.J.; Yang, T. The Gravitational-Wave Physics. *Natl. Sci. Rev.* **2017**, *4*, 687–706. [CrossRef]
28. Caprini, C.; Chala, M.; Dorsch, G.C.; Hindmarsh, M.; Huber, S.J.; Konstandin, T.; Kozaczuk, J.; Nardini, G.; No, J.M.; Rummukainen, K.; et al. Detecting gravitational waves from cosmological phase transitions with LISA: An update. *J. Cosmol. Astropart. Phys.* **2020**, *3*, 24. [CrossRef]
29. Hindmarsh, M.B.; Lüben, M.; Lumma, J.; Pauly, M. Phase transitions in the early universe. *SciPost Phys. Lect. Notes* **2021**, *24*, 1. [CrossRef]
30. Bian, L.; Cai, R.-G.; Cao, S.; Cao, Z.; Gao, H.; Guo, Z.-K.; Lee, K.; Li, D.; Liu, J.; Lu, Y.; et al. The Gravitational-wave physics II: Progress. *Sci. China Phys. Mech. Astron.* **2021**, *64*, 120401. [CrossRef]
31. D'Onofrio, M.; Rummukainen, K.; Tranberg, A. Sphaleron Rate in the Minimal Standard Model. *Phys. Rev. Lett.* **2014**, *113*, 141602. [CrossRef]
32. Athron, P.; Balazs, C.; Fowlie, A.; Pozzo, G.; White, G.; Zhang, Y. Strong first-order phase transitions in the NMSSM—A comprehensive survey. *J. High Energy Phys.* **2019**, *11*, 151. [CrossRef]
33. Han, X.F.; Wang, L.; Zhang, Y. Dark matter, electroweak phase transition, and gravitational waves in the type II two-Higgs-doublet model with a singlet scalar field. *Phys. Rev. D* **2021**, *103*, 035012. [CrossRef]
34. Xiao, Y.; Yang, J.M.; Zhang, Y. Implications of nano-Hertz gravitational waves on electroweak phase transition in the singlet dark matter model. *Sci. Bull.* **2023**, *68*, 3158–3164. [CrossRef] [PubMed]
35. Si, Z.-g.; Wang, H.-x.; Wang, L.; Zhang, Y. Exploring multi-step electroweak phase transitions in the 2HDM+*a*. *Eur. Phys. J. C* **2025**, *85*, 273. [CrossRef]
36. Li, S.; Yang, J.M.; Zhang, M.; Zhang, Y.; Zhu, R. Can a secluded self-interacting dark sector generate detectable gravitational waves? *arXiv* **2025**, arXiv:2502.04108. [CrossRef]
37. Guan, S.; Guo, H.K.; Jiao, D.; Liang, Q.; Wu, L.; Zhang, Y. Measuring Gravitational Wave Spectrum from Electroweak Phase Transition and Higgs Self-Couplings. *arXiv* **2025**, arXiv:2511.00996. [CrossRef]
38. Trodden, M. Electroweak baryogenesis. *Rev. Mod. Phys.* **1999**, *71*, 1463–1500. [CrossRef]
39. Morrissey, D.E.; Ramsey-Musolf, M.J. Electroweak baryogenesis. *New J. Phys.* **2012**, *14*, 125003. [CrossRef]
40. Biekötter, T.; Heinemeyer, S.; Weiglein, G. Vacuum (meta-)stability in the $\mu\nu$SSM. *Eur. Phys. J. C* **2022**, *82*, 301. [CrossRef]

41. Biekötter, T.; Heinemeyer, S.; No, J.M.; Olea-Romacho, M.O.; Weiglein, G. The trap in the early Universe: Impact on the interplay between gravitational waves and LHC physics in the 2HDM. *J. Cosmol. Astropart. Phys.* **2023**, *3*, 31. [CrossRef]
42. Arsenault, A.; Cingiloglu, K.Y.; Frank, M. Vacuum stability in the Standard Model with vectorlike fermions. *Phys. Rev. D* **2023**, *107*, 036018. [CrossRef]
43. Balázs, C.; Xiao, Y.; Yang, J.M.; Zhang, Y. New vacuum stability limit from cosmological history. *Nucl. Phys. B* **2024**, *1002*, 116533. [CrossRef]
44. Wainwright, C.; Profumo, S. The Impact of a strongly first-order phase transition on the abundance of thermal relics. *Phys. Rev. D* **2009**, *80*, 103517. [CrossRef]
45. Baker, M.J.; Kopp, J.; Long, A.J. Filtered Dark Matter at a First Order Phase Transition. *Phys. Rev. Lett.* **2020**, *125*, 151102. [CrossRef] [PubMed]
46. Baker, M.J.; Kopp, J. Dark Matter Decay between Phase Transitions at the Weak Scale. *Phys. Rev. Lett.* **2017**, *119*, 061801. [CrossRef] [PubMed]
47. Baker, M.J.; Mittnacht, L. Variations on the Vev Flip-Flop: Instantaneous Freeze-out and Decaying Dark Matter. *J. High Energy Phys.* **2019**, *5*, 70. [CrossRef]
48. Bian, L.; Liu, X. Two-step strongly first-order electroweak phase transition modified FIMP dark matter, gravitational wave signals, and the neutrino mass. *Phys. Rev. D* **2019**, *99*, 055003. [CrossRef]
49. Wong, X.R.; Xie, K.P. Freeze-in of WIMP dark matter. *Phys. Rev. D* **2023**, *108*, 055035. [CrossRef]
50. Chung, D.; Long, A.; Wang, L.T. Probing the Cosmological Constant and Phase Transitions with Dark Matter. *Phys. Rev. D* **2011**, *84*, 043523. [CrossRef]
51. Xiao, Y.; Yang, J.M.; Zhang, Y. Dilution of dark matter relic density in singlet extension models. *J. High Energy Phys.* **2023**, *2*, 8. [CrossRef]
52. Roy, S. Dilution of dark matter relic abundance due to first order electroweak phase transition in the singlet scalar extended type-II seesaw model. *Phys. Rev. D* **2025**, *111*, 015037. [CrossRef]
53. Wang, W.; Xu, W.L.; Yang, J.M. A hidden self-interacting dark matter sector with first-order cosmological phase transition and gravitational wave. *Eur. Phys. J. Plus* **2023**, *138*, 781. [CrossRef]
54. Wainwright, C.L. CosmoTransitions: Computing Cosmological Phase Transition Temperatures and Bubble Profiles with Multiple Fields. *Comput. Phys. Commun.* **2012**, *183*, 2006–2013. [CrossRef]
55. Basler, P.; Mühlleitner, M. BSMPT (Beyond the Standard Model Phase Transitions): A tool for the electroweak phase transition in extended Higgs sectors. *Comput. Phys. Commun.* **2019**, *237*, 62–85. [CrossRef]
56. Basler, P.; Mühlleitner, M.; Müller, J. BSMPT v2 a tool for the electroweak phase transition and the baryon asymmetry of the universe in extended Higgs Sectors. *Comput. Phys. Commun.* **2021**, *269*, 108124. [CrossRef]
57. Basler, P.; Biermann, L.; Mühlleitner, M.; Müller, J.; Santos, R.; Viana, J. BSMPT v3 a tool for phase transitions and primordial gravitational waves in extended Higgs sectors. *Comput. Phys. Commun.* **2025**, *316*, 109766. [CrossRef]
58. Athron, P.; Balázs, C.; Fowlie, A.; Zhang, Y. PhaseTracer: Tracing cosmological phases and calculating transition properties. *Eur. Phys. J. C* **2020**, *80*, 567. [CrossRef]
59. Athron, P.; Balazs, C.; Fowlie, A.; Morris, L.; Searle, W.; Xiao, Y.; Zhang, Y. PhaseTracer2: From the effective potential to gravitational waves. *Eur. Phys. J. C* **2025**, *85*, 559. [CrossRef]
60. Ertas, F.; Kahlhoefer, F.; Tasillo, C. Turn up the volume: Listening to phase transitions in hot dark sectors. *J. Cosmol. Astropart. Phys.* **2022**, *2*, 14. [CrossRef]
61. Brdar, V.; Finetti, M.; Matteini, M.; Morais, A.P.; Nemevšek, M. PT2GWFinder: A Package for Cosmological First-Order Phase Transitions and Gravitational Waves. *arXiv* **2025**, arXiv:2505.04744. [CrossRef]
62. Costa, F.; Hoefken Zink, J.; Lucente, M.; Pascoli, S.; Rosauro-Alcaraz, S. ELENA: A software for fast and precise computation of first order phase transitions and gravitational waves production in particle physics models. *arXiv* **2025**, arXiv:2510.00289. [CrossRef]
63. Masoumi, A.; Olum, K.D.; Shlaer, B. Efficient numerical solution to vacuum decay with many fields. *J. Cosmol. Astropart. Phys.* **2017**, *1*, 51. [CrossRef]
64. Athron, P.; Balázs, C.; Bardsley, M.; Fowlie, A.; Harries, D.; White, G. BubbleProfiler: Finding the field profile and action for cosmological phase transitions. *Comput. Phys. Commun.* **2019**, *244*, 448–468. [CrossRef]
65. Sato, R. SimpleBounce: A simple package for the false vacuum decay. *Comput. Phys. Commun.* **2021**, *258*, 107566. Erratum in *Comput. Phys. Commun.* **2026**, *320*, 110006. [CrossRef]
66. Guada, V.; Nemevšek, M.; Pintar, M. FindBounce: Package for multi-field bounce actions. *Comput. Phys. Commun.* **2020**, *256*, 107480. [CrossRef]
67. Camargo-Molina, J.E.; O'Leary, B.; Porod, W.; Staub, F. Vevacious: A Tool For Finding The Global Minima of One-Loop Effective Potentials With Many Scalars. *Eur. Phys. J. C* **2013**, *73*, 2588. [CrossRef]
68. Fowlie, A. A fast C++ implementation of thermal functions. *Comput. Phys. Commun.* **2018**, *228*, 264–272. [CrossRef]

69. Ekstedt, A.; Schicho, P.; Tenkanen, T.V.I. DRalgo: A package for effective field theory approach for thermal phase transitions. *Comput. Phys. Commun.* **2023**, *288*, 108725. [CrossRef]
70. Ekstedt, A.; Gould, O.; Hirvonen, J.; Laurent, B.; Niemi, L.; Schicho, P.; van de Vis, J. How fast does the WallGo? A package for computing wall velocities in first-order phase transitions. *J. High Energy Phys.* **2025**, *4*, 101. [CrossRef]
71. van de Vis, J.; Schicho, P.; Niemi, L.; Laurent, B.; Hirvonen, J.; Gould, O. WallGo investigates: Theoretical uncertainties in the bubble wall velocity. *arXiv* **2025**, arXiv:2510.27691. [CrossRef]
72. Ekstedt, A.; Gould, O.; Hirvonen, J. BubbleDet: A Python package to compute functional determinants for bubble nucleation. *J. High Energy Phys.* **2023**, *12*, 56. [CrossRef]
73. Si, Z.; Wang, H.; Wang, L.; Xiao, Y.; Zhang, Y. The bubble wall velocity in local thermal equilibrium and energy budget with full effective potential. *J. High Energy Phys.* **2025**, *2025*, 29. [CrossRef]
74. Patel, H.H.; Ramsey-Musolf, M.J. Baryon Washout, Electroweak Phase Transition, and Perturbation Theory. *J. High Energy Phys.* **2011**, *7*, 29. [CrossRef]
75. Athron, P.; Balazs, C.; Fowlie, A.; Morris, L.; White, G.; Zhang, Y. How arbitrary are perturbative calculations of the electroweak phase transition? *J. High Energy Phys.* **2023**, *2023*, 50. [CrossRef]
76. Sher, M. Electroweak Higgs potential and vacuum stability. *Phys. Rep.* **1989**, *179*, 273–418. [CrossRef]
77. Quiros, M. Finite temperature field theory and phase transitions. In *Proceedings of the ICTP Summer School in High-Energy Physics and Cosmology*; World Scientific: Singapore, 1999; pp. 187–259.
78. Zinn-Justin, J. Quantum field theory at finite temperature: An Introduction. *arXiv* **2000**, arXiv:hep-ph/0005272. [CrossRef]
79. Laine, M.; Vuorinen, A. *Basics of Thermal Field Theory*; Springer: Berlin/Heidelberg, Germany, 2016; Volume 925. [CrossRef]
80. Parwani, R.R. Resummation in a hot scalar field theory. *Phys. Rev. D* **1992**, *45*, 4695. Erratum in *Phys. Rev. D* **1993**, *48*, 5965. [CrossRef]
81. Arnold, P.B.; Espinosa, O. The Effective potential and first order phase transitions: Beyond leading-order. *Phys. Rev. D* **1993**, *47*, 3546. Erratum in *Phys. Rev. D* **1994**, *50*, 6662. [CrossRef]
82. Appelquist, T.; Pisarski, R.D. High-temperature Yang-Mills theories and three-dimensional quantum chromodynamics. *Phys. Rev. D* **1981**, *23*, 2305–2317. [CrossRef]
83. Ginsparg, P. First and second order phase transitions in gauge theories at finite temperature. *Nucl. Phys. B* **1980**, *170*, 388–408. [CrossRef]
84. Laine, M.; Meyer, M.; Nardini, G. Thermal phase transition with full 2-loop effective potential. *Nucl. Phys. B* **2017**, *920*, 565–600. [CrossRef]
85. Ekstedt, A.; Löfgren, J. A Critical Look at the Electroweak Phase Transition. *J. High Energy Phys.* **2020**, *12*, 136. [CrossRef]
86. Kainulainen, K.; Keus, V.; Niemi, L.; Rummukainen, K.; Tenkanen, T.V.I.; Vaskonen, V. On the validity of perturbative studies of the electroweak phase transition in the Two Higgs Doublet model. *J. High Energy Phys.* **2019**, *2019*, 75. [CrossRef]
87. Wolfram Research, I. Mathematica 14.0. 2024. Available online: https://www.wolfram.com/mathematica/ (accessed on 20 February 2026).
88. Staub, F. Exploring new models in all detail with SARAH. *Adv. High Energy Phys.* **2015**, *2015*, 840780. [CrossRef]
89. Virtanen, P.; Gommers, R.; Oliphant, T.E.; Haberland, M.; Reddy, T.; Cournapeau, D.; Burovski, E.; Peterson, P.; Weckesser, W.; Bright, J.; et al. *SciPy 1.0: Fundamental Algorithms for Scientific Computing in Python*; Nature Research: London, UK, 2020. [CrossRef]
90. Fowlie, A. thermal_funcs: Thermal Functions for Finite-Temperature Effective Field-Theory in C++ with Python and Mathematica Interfaces. GitHub Repository, 2024. Available online: https://github.com/andrewfowlie/thermal_funcs (accessed on 20 February 2026).
91. Piessens, R.; de Doncker-Kapenga, E.; Überhuber, C.; Kahaner, D. *QUADPACK: A Subroutine Package for Automatic Integration*; Springer Series in Computational Mathematics; Springer: Berlin/Heidelberg, Germany, 1983; Volume 1. [CrossRef]
92. Coimbra, R.; Sampaio, M.O.P.; Santos, R. ScannerS: Constraining the phase diagram of a complex scalar singlet at the LHC. *Eur. Phys. J. C* **2013**, *73*, 2428. [CrossRef]
93. Biekötter, T.; Olea-Romacho, M.O. Benchmarking a fading window: Electroweak baryogenesis in the C2HDM, LHC constraints after Run 2 and prospects for LISA. *J. High Energy Phys.* **2025**, *2025*, 40. [CrossRef]
94. Biekötter, T.; Grohsjean, A.; Heinemeyer, S.; Schwanenberger, C.; Weiglein, G. Possible indications for new Higgs bosons in the reach of the LHC: N2HDM and NMSSM interpretations. *Eur. Phys. J. C* **2022**, *82*, 178. [CrossRef]
95. Del Cima, O.M.; Franco, D.H.T.; Piguet, O. Gauge independence of the effective potential revisited. *Nucl. Phys. B* **1999**, *551*, 813–825. [CrossRef]
96. Nielsen, N. On the gauge dependence of spontaneous symmetry breaking in gauge theories. *Nucl. Phys. B* **1975**, *101*, 173–188. [CrossRef]
97. Del Cima, O.M. Probing the Nielsen identities. *Phys. Lett. B* **1999**, *457*, 307–310. [CrossRef]

98. Nielsen, N.K. Removing the gauge parameter dependence of the effective potential by a field redefinition. *Phys. Rev. D* **2014**, *90*, 036008. [CrossRef]
99. Di Luzio, L.; Mihaila, L. On the gauge dependence of the Standard Model vacuum instability scale. *J. High Energy Phys.* **2014**, *2014*, 79. [CrossRef]
100. Espinosa, J.R.; Garny, M.; Konstandin, T. Interplay of Infrared Divergences and Gauge-Dependence of the Effective Potential. *Phys. Rev. D* **2016**, *94*, 055026. [CrossRef]
101. Athron, P.; Bach, M.; Harries, D.; Kwasnitza, T.; Park, J.h.; Stöckinger, D.; Voigt, A.; Ziebell, J. FlexibleSUSY 2.0: Extensions to investigate the phenomenology of SUSY and non-SUSY models. *Comput. Phys. Commun.* **2018**, *230*, 145–217. [CrossRef]
102. Searle, W.; Balázs, C.; Xiao, Y.; Zhang, Y. Machine learning left-right breaking from gravitational waves. *J. Cosmol. Astropart. Phys.* **2025**, *11*, 34. [CrossRef]
103. Vaskonen, V. Electroweak baryogenesis and gravitational waves from a real scalar singlet. *Phys. Rev. D* **2017**, *95*, 123515. [CrossRef]
104. Nelder, J.A.; Mead, R. A Simplex Method for Function Minimization. *Comput. J.* **1965**, *7*, 308–313. [CrossRef]
105. Moore, G.D. Measuring the broken phase sphaleron rate nonperturbatively. *Phys. Rev. D* **1999**, *59*, 014503. [CrossRef]
106. Linde, A.D. Fate of the false vacuum at finite temperature: Theory and applications. *Phys. Lett. B* **1981**, *100*, 37–40. [CrossRef]
107. Linde, A. Decay of the false vacuum at finite temperature. *Nucl. Phys. B* **1983**, *223*, 544. [CrossRef]
108. Akula, S.; Balázs, C.; White, G.A. Semi-analytic techniques for calculating bubble wall profiles. *Eur. Phys. J. C* **2016**, *76*, 681. [CrossRef]
109. Andreassen, A.; Farhi, D.; Frost, W.; Schwartz, M.D. Direct Approach to Quantum Tunneling. *Phys. Rev. Lett.* **2016**, *117*, 231601. [CrossRef]
110. Brown, A.R. Thin-wall approximation in vacuum decay: A lemma. *Phys. Rev. D* **2018**, *97*, 105002. [CrossRef]
111. Espinosa, J.R.; Konstandin, T. A Fresh Look at the Calculation of Tunneling Actions in Multi-Field Potentials. *J. Cosmol. Astropart. Phys.* **2019**, *1*, 51. [CrossRef]
112. Espinosa, J.R. A Fresh Look at the Calculation of Tunneling Actions. *J. Cosmol. Astropart. Phys.* **2018**, *7*, 36. [CrossRef]
113. Braden, J.; Johnson, M.C.; Peiris, H.V.; Pontzen, A.; Weinfurtner, S. New Semiclassical Picture of Vacuum Decay. *Phys. Rev. Lett.* **2019**, *123*, 031601. Erratum in *Phys. Rev. Lett.* **2022**, *129*, 059901. [CrossRef] [PubMed]
114. Piscopo, M.L.; Spannowsky, M.; Waite, P. Solving differential equations with neural networks: Applications to the calculation of cosmological phase transitions. *Phys. Rev. D* **2019**, *100*, 016002. [CrossRef]
115. Sato, R. Simple Gradient Flow Equation for the Bounce Solution. *Phys. Rev. D* **2020**, *101*, 016012. [CrossRef]
116. Bardsley, M. An optimisation based algorithm for finding the nucleation temperature of cosmological phase transitions. *Comput. Phys. Commun.* **2022**, *273*, 108252. [CrossRef]
117. Coleman, S. Erratum: Fate of the false vacuum: Semiclassical theory. *Phys. Rev. D* **1977**, *16*, 1248. [CrossRef]
118. Cline, J.M.; Moore, G.D.; Servant, G. Was the electroweak phase transition preceded by a color broken phase? *Phys. Rev. D* **1999**, *60*, 105035. [CrossRef]
119. Guada, V.; Maiezza, A.; Nemevšek, M. Multifield Polygonal Bounces. *Phys. Rev. D* **2019**, *99*, 056020. [CrossRef]
120. Jinno, R. Machine learning for bounce calculation. *arXiv* **2018**, arXiv:1805.12153 . [CrossRef]
121. Bian, L.; Wang, H.; Xiao, Y.; Yang, J.C.; Yang, J.M.; Zhang, Y. Enhancing Phase Transition Calculations with Fitting and Neural Network. *arXiv* **2025**, arXiv:2510.10667. [CrossRef]
122. Callan, C.G.; Coleman, S. Fate of the false vacuum. II. First quantum corrections. *Phys. Rev. D* **1977**, *16*, 1762–1768. [CrossRef]
123. Guth, A.H.; Tye, S.H.H. Phase Transitions and Magnetic Monopole Production in the Very Early Universe. *Phys. Rev. Lett.* **1980**, *44*, 631–635. [CrossRef]
124. Guth, A.H.; Weinberg, E.J. Cosmological consequences of a first-order phase transition in the SU_5 grand unified model. *Phys. Rev. D* **1981**, *23*, 876–885. [CrossRef]
125. Athron, P.; Balázs, C.; Morris, L. Supercool subtleties of cosmological phase transitions. *J. Cosmol. Astropart. Phys.* **2023**, *3*, 6. [CrossRef]
126. Ellis, J.; Lewicki, M.; No, J.M. On the Maximal Strength of a First-Order Electroweak Phase Transition and its Gravitational Wave Signal. *J. Cosmol. Astropart. Phys.* **2019**, *4*, 3. [CrossRef]
127. Lewicki, M.; Merchand, M.; Zych, M. Electroweak bubble wall expansion: Gravitational waves and baryogenesis in Standard Model-like thermal plasma. *J. High Energy Phys.* **2022**, *2022*, 17. [CrossRef]
128. Ellis, J.; Lewicki, M.; Merchand, M.; No, J.M.; Zych, M. The scalar singlet extension of the Standard Model: Gravitational waves versus baryogenesis. *J. High Energy Phys.* **2023**, *2023*, 93. [CrossRef]
129. Laurent, B.; Cline, J.M. First principles determination of bubble wall velocity. *Phys. Rev. D* **2022**, *106*, 023501. [CrossRef]
130. Espinosa, J.R.; Konstandin, T.; No, J.M.; Servant, G. Energy Budget of Cosmological First-order Phase Transitions. *J. Cosmol. Astropart. Phys.* **2010**, *6*, 28. [CrossRef]

131. Hindmarsh, M.; Huber, S.J.; Rummukainen, K.; Weir, D.J. Numerical simulations of acoustically generated gravitational waves at a first order phase transition. *Phys. Rev. D* **2015**, *92*, 123009. [CrossRef]
132. Caprini, C.; Durrer, R.; Servant, G. The stochastic gravitational wave background from turbulence and magnetic fields generated by a first-order phase transition. *J. Cosmol. Astropart. Phys.* **2009**, *12*, 24. [CrossRef]
133. Hindmarsh, M. Sound shell model for acoustic gravitational wave production at a first-order phase transition in the early Universe. *Phys. Rev. Lett.* **2018**, *120*, 071301. [CrossRef]
134. Hindmarsh, M.; Huber, S.J.; Rummukainen, K.; Weir, D.J. Shape of the acoustic gravitational wave power spectrum from a first order phase transition. *Phys. Rev. D* **2017**, *96*, 103520. Erratum in *Phys. Rev. D* **2020**, *101*, 089902. [CrossRef]
135. Gowling, C.; Hindmarsh, M.; Hooper, D.C.; Torrado, J. Reconstructing physical parameters from template gravitational wave spectra at LISA: First order phase transitions. *J. Cosmol. Astropart. Phys.* **2023**, *4*, 61. [CrossRef]
136. Lewicki, M.; Vaskonen, V. Gravitational waves from bubble collisions and fluid motion in strongly supercooled phase transitions. *Eur. Phys. J. C* **2023**, *83*, 109. [CrossRef]
137. Dahl, J.; Hindmarsh, M.; Rummukainen, K.; Weir, D.J. Primordial acoustic turbulence: Three-dimensional simulations and gravitational wave predictions. *Phys. Rev. D* **2024**, *110*, 103512. [CrossRef]
138. Figueroa, D.G.; Florio, A.; Torrenti, F.; Valkenburg, W. CosmoLattice: A modern code for lattice simulations of scalar and gauge field dynamics in an expanding universe. *Comput. Phys. Commun.* **2023**, *283*, 108586. [CrossRef]
139. Huang, Z. Art of lattice and gravity waves from preheating. *Phys. Rev. D* **2011**, *83*, 123509. [CrossRef]
140. Easther, R.; Finkel, H.; Roth, N. PSpectRe: A Pseudo-Spectral Code for (P)reheating. *J. Cosmol. Astropart. Phys.* **2010**, *10*, 25. [CrossRef]